Supporting Information

Supporting Information Corrected October 27, 2014
Kim et al. 10.1073/pnas.1405209111

SI Materials and Methods

Reagents. ATP (adenosine-5′-triphosphate 1G; Fisher Scientific) used for stimulation was diluted with Danilchik's For Amy solution (DFA) to the appropriate concentrations (1–500 μM). The blebbistatin (BBS, Sigma-Aldrich) used for inhibiting actomyosin activity was first prepared in aliquots of 100 mM dissolved in dimethyl sulfoxide (DMSO, Sigma-Aldrich) and then diluted with DFA to a final concentration of 100 μM. The heptanol (HEP, Sigma-Aldrich) used to inhibit gap junctions was first prepared in aliquots of 0.5 mM and diluted with DFA for a final concentration of 5 nM.

Microscopy and Image Analysis. Embryo responses were imaged with a digital CCD camera (Scion Corp.) mounted on a stereomicroscope (SZX12, Olympus Corp.). Live-cell confocal time-lapse sequences were collected using a laser scanning confocal microscope mounted on an inverted compound microscope (Leica TCS SP5; Leica Microsystems). The image acquisition and subsequent analysis of time-lapses sequences used custom-written macros and plug-ins and image analysis software (ImageJ ver. 1.43, Wayne Rasband, National Institutes of Health) (http://imagej.nih.gov/ij). As ATP visualization was extremely important, to visualize ATP solutions, 3 μL black ink (Higgins Fountain Pen India Ink; Utrecht Art) was added to a 50-mL central reservoir.

Microfluidic Device Design. Modular microfluidic devices were fabricated using soft lithography (1) with polydimethylsiloxane (SYLGARD 184, Dow Corning). The microfluidic devices for modular resistances (R20-100 × 50) and (R60-100 × 50) were 20 and 60 mm long, respectively, and had cross-sections that were 100 μm wide and 50 μm high. The microfluidic channel for the animal cap (AC) explants had three inlet channels that were rectangular cross-sections with dimensions 500 μm wide, 300 μm high, and 5 mm long. The central inlet was used in part as a temporary outlet for removing air bubbles in the fluidic network before the experiments; these bubbles would disrupt the experiment. These inlet channels converged to form a single outlet channel (rectangular cross-section 1500 μm wide, 300 μm high, and 10 mm long). The reservoirs and pressure sensors were connected to the microfluidic device using polyethylene tubing (Intramedic, inner diameter of 0.78 mm). To introduce the explants into the microfluidic channels, a negative pressure was applied to the microfluidic channel outlet. This procedure enabled the explants to be drawn in and then allowed them to adhere to the glass substrate, which was the bottom surface of the microfluidic channel; this surface first was coated with fibronectin.

Control System Configuration. The control system regulated the pressure and thus the flow rate at the outer streams in the microfluidic system. A discrete-time proportional-integral-derivative (PID) pressure controller and a proportional-derivative (PD) position controller were integrated with a PIC micro 18F4620 microcontroller (Peripheral Interface Controller, Microchip Technology, Inc.) at a sampling rate of 125 Hz. A PID controller is a generic control loop feedback mechanism that involves three separate constant parameters: the proportional, integral, and derivative values, denoted P, I, and D, respectively. These values can be interpreted in terms of time: P depends on the present error, I on the accumulation of past errors, and D is a prediction of future errors, based on current rate of change. The sampling rate was determined by the maximum response time (8 ms) of the piezoelectric gauge pressure sensor (ASDX series, Honeywell International Inc.). This microcontroller sent pulse-width-modulation signals and regulated the angle of the direct-current (DC) electric motor through an encoder with a resolution of 512 counts per revolution.

Response to Frequency Stimulation. The development of embryonic tissues is a tightly correlated response to both spatial and temporal cues, which are related to chemical and mechanical factors in a frequency-based manner. To investigate a role of stimulation frequency in producing distinct responses, we implemented periodically adjustable, localized stimulation with 100-μm-wide ATP streams: negative stimulation (NS; Fig. S9*A*); 10-s period (0.1 cycle/s frequency; Fig. S9*B*); 40-s period (0.025 cycle/s frequency; Fig. S9*C*); 80-s period (0.0125 cycle/s frequency; Fig. S9*D*); and continuous stimulation (CS; Fig. S9*E*). The oscillatory response was found at a lower frequency of 0.0125 cycle/s (Fig. S9*D*) but not at higher frequencies (Fig. S9 *B* and *C*) exhibiting smooth contractility profiles. These results suggest that there may be limited relaxation during the "off" stimulation, which would be correlated to 20 and 40 s of no stimulation. When the period of "off" stimulation is 80 s, the relaxation may have an opportunity to begin before the next "on" stimulation because the cells are not stimulated again in the next "on" period. In addition, more cells could have been brought into contact with the ATP stream as the cells in the ATP contracted, which would bring new unstimulated cells into the ATP stimulated region. This propagating event (more cells contracting bringing in new cells that would contract themselves and bring in new cells) would become more pronounced with longer duty cycles, which would allow this propagating event to develop further. This potential response may be implied in the cutoff frequency response. Investigation of the responses to periodic stimulation revealed a set of distinctive time constants that could be used to reconstruct the dynamics of the actuator mediating the ATP stimulation and contraction response. We found an ∼20-s time delay (τ_d) before rapid contraction with an ∼30-s time constant (τ_{rise}) followed by slow relaxation with an ∼50-s time constant (τ_{relax}). This behavior in an actuator occurs as long as the stimulation profile is periodic in the form of a pulse (Figs. S3 and S9). To simulate dynamical response of an ATP stimulated tissue we constructed a low-order linear time-invariant system model. The model reproduced contraction responses to 20-s stimuli under both single-pulse and periodic profiles (Figs. S3 and S9*F*). The qualitative agreement suggests that the input–output response of a complex multicellular tissue to complex patterns of stimulation could be deterministic and predictably controlled by a systems-based modeling framework.

Determination of Model Parameters. A response to 20-s pulse stimulations was determined, which led to a second-order "gray-box" process model with two different time constants. A more complete model included a time-delay component from the result of the distinct time response and is given by

$$F(s) = e^{-\tau_d s}\frac{K_{DC}}{(\tau_{rise}\cdot s+1)(\tau_{relax}\cdot s+1)}U(s),$$

where $F(s)$ is the Laplace transform of the displacement of the spatial maximum cell contraction $f(t)$, τ_d represents the delay of the response, τ_{rise} is the time constant responsible for the rapid contraction, and τ_{relax} is the time constant for the slow relaxation. These two time constants represent the characteristic response

frequencies. The DC gain, K_{DC}, is used to represent a scaling factor from the input to the output and $U(s)$ is the Laplace transform of time-varying ATP exposure, $u(t)$, in terms of the concentration. We obtained the response of the contraction profile as a function of time through an inverse Laplace transformation as below.

$$L^{-1}\left(F(s)\right) = f(t) = \frac{K_{DC}}{\tau_{rise} - \tau_{relax}} \cdot \left(e^{\frac{-(t-\tau_d)}{\tau_{rise}}} - e^{\frac{-(t-\tau_d)}{\tau_{relax}}} \right) \cdot u(t).$$

Therefore, the transfer function $G(s)$ of the contraction to ATP stimulation and its time domain form is

$$G(s) = \frac{F(s)}{U(s)} = e^{-\tau_d S} \frac{K_{DC}}{(\tau_{rise} \cdot s + 1)(\tau_{relax} \cdot s + 1)}$$

$$g(t) = \frac{K_{DC}}{\tau_{rise} - \tau_{relax}} \cdot \left(e^{\frac{-(t-\tau_d)}{\tau_{rise}}} - e^{\frac{-(t-\tau_d)}{\tau_{relax}}} \right).$$

Because the time derivative of $g(t)$ equals zero when it reaches a maximum value, the time to reach the maximum contraction in the time domain is

$$t_{\max} = \tau_d + \frac{1}{\frac{1}{\tau_{rise}} - \frac{1}{\tau_{relax}}} \ln \frac{\tau_{relax}}{\tau_{rise}}.$$

As time goes to infinity, the effect of the rising exponential term on the response profile is negligible, so the time derivative of $g(t)$ simplifies to

$$\ln g(t) = \ln \frac{K_{DC}}{\tau_{relax} - \tau_{rise}} - \frac{t - \tau_d}{\tau_{relax}}.$$

The best-fit values of the time constants and the gain were determined through iterative estimation. Thus, these model parameters were determined through comparing the response to 20-s pulse stimulation with the asymptotic line. Through this approach, the two time constants τ_{rise}~30 s, τ_{relax}~50 s, along with the DC gain K_{DC} = 1.6E6, were determined.

Computation Fluid Dynamics. Numerical simulations of the flow field were conducted using the commercial computation fluid dynamics solver (Fluent, ANSYS Inc.) to solve the nonlinear Navier–Stokes equations governing the conservation of mass and momentum within the fluid elements. Advection–diffusion equations were also solved to predict the flow field and the user-defined scalar species. We assumed a Newtonian fluid having the properties of water at room temperature and no-slip boundary conditions on all of the walls. Mesh independence was verified by examining higher density meshes. The SIMPLE algorithm was implemented for pressure–velocity coupling and spatial discretization was performed using the second-order upwind scheme. In computational approaches, upwind schemes are one of the numerical discretization methods related to finite difference methods for solving partial differential equations. The spatial accuracy of the first-order upwind scheme can be improved by including three data points instead of just two in the first order, which offers a more accurate finite difference for the approximation of the spatial derivative. Flow rates were specified at the five inlets that were correlated to the applied inlet pressures in the experiments along with using atmospheric pressure at the outlet. Convergence limits were set so that velocities converged within 0.1% and mass fractions for the central stream species reached their asymptotic values within 0.01%.

Finite Element Model. We created a static structure finite element (FE) model of embryonic tissue using commercial software (ANSYS V.14.0) to predict the elastic strain of the outermost layer exposed to a stream of ATP. The 3D physical model was composed of three different layers (apical, epithelial, and deep cells) that are purely bonded and no penetration is allowed. The mesh had ~170,000 tetrahedral elements with 300,000 nodes. To predict the response of contractility, the embryonic tissue was assumed as an initially circular disk block composed of the apical layer (1 μm thick), the epithelial layer (10 μm thick), and the deep cell layer (100 μm thick). We assumed the thermal expansion was related to the change in temperature applied to the block where the ATP stream presented. Because our mechanochemical actuator testing of AC tissue appeared to be related to the deformation of mechanical properties, we used an elastic structure with one-term Ogden material (2) to investigate how the patterns of deformation varied with temperature. In addition, we assumed it was an isotropic and nearly incompressible (Poisson; ν = 0.499) material to characterize the volumetric strain ϱ_T, which was linearly proportional to the change in temperature and given by the relation

$$\varrho_T = (1 + \alpha\Delta T)^3 - 1 \approx 3\alpha\Delta T = \beta\Delta T,$$

where the coefficient of proportionality β was the volumetric coefficient of thermal expansion being 0.001 and a sinusoidal temperature ranging from ~22 °C to −300 °C was applied. Initially, the central region was at 22 °C. This condition was only implied to the apical cell-layer block where the ATP was presented whereas the other layers had thermal coefficients of zero. Many soft tissues are considered as roughly incompressible materials and assumed to have a Poisson ratio of ν = 0.499 with Young's modulus of 10 Pa (3). In the FE model, we found that the normal stiffness factor between the layers of assembled multilayer tissue structures was a critical factor when simulating the contractility. According to the FE model vendor, this factor biases the way strain energy was calculated, meaning that the low values emphasize bending energy whereas high values emphasize bulk. The normal stiffness factor drove the apical surface to then contract more in the z direction (out of the plane) and caused the tissue to expand in the x- and y directions. In addition, the transmission distance appeared in a function of the mechanical properties of the tissue based on this model and thus the displacement decreased at further points similar to what naturally occurs in viscoelastic materials (3).

Statistical Analyses. Statistical analyses for verifying the significance of the intensity ratio values were carried out with nonparametric Mann–Whitney u tests using commercial software, Minitab (Minitab Inc.). The differences were considered significant at a value of $P < 0.05$.

1. Kim E, Xia YN, Whitesides GM (1995) Polymer microstructures formed by molding in capillaries. *Nature* 376(6541):581–584.
2. Holzapfel G (2001) Biomechanics of soft tissue. *The Handbook of Materials Behavior Models*, ed Lemaitre J (Academic, Boston), Vol 3, pp 1049–1063.
3. von Dassow M, Strother JA, Davidson LA (2010) Surprisingly simple mechanical behavior of a complex embryonic tissue. *PLoS ONE* 5(12):e15359.
4. Zhou J, Kim HY, Davidson LA (2009) Actomyosin stiffens the vertebrate embryo during crucial stages of elongation and neural tube closure. *Development* 136(4):677–688.

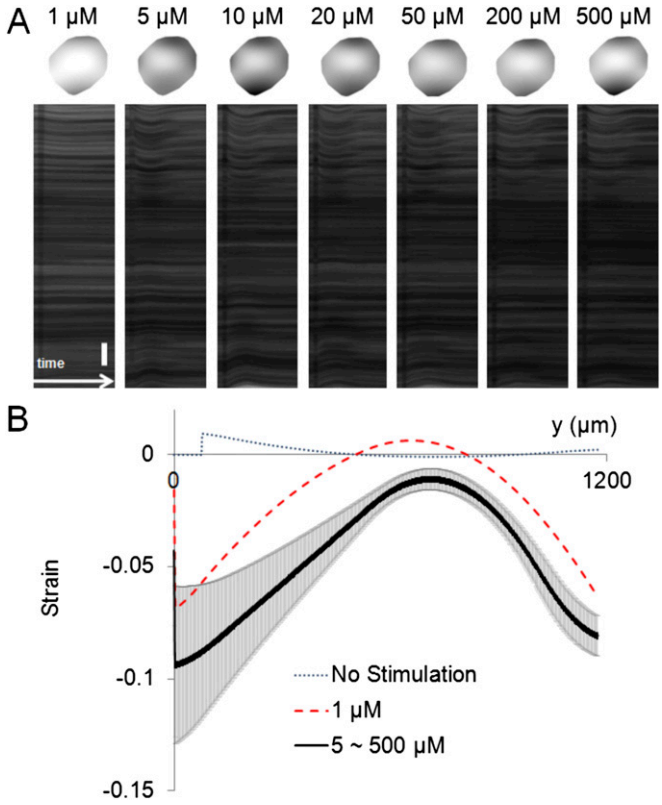

Fig. S1. Extracellular ATP with concentrations greater than 5 μM induces quantitatively similar contraction responses in a tissue. (*A*) Strain maps in tissues that were cultured in microfluidic channel and entirely stimulated for 20 s with extracellular ATP streams with a range of concentrations from 1 to 500 μM. Experiments were independently conducted with a 5-min break between tests. Kymographs showed quantitatively similar contraction responses to streams of ATP (>5 μM). (Scale bar: 100 μm.) (*B*) Strain distributions in the tissue shown in *A*, which show the quantitatively similar results for the ATP concentration ranges of 5–500 μM.

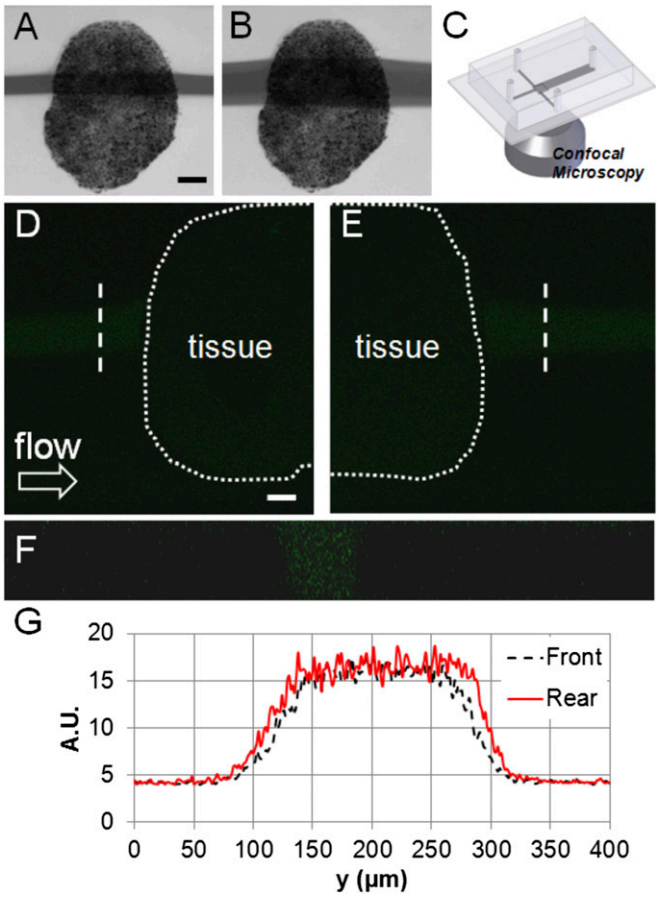

Fig. S2. Sharp concentration gradient profile across the interface in front of and behind the tissue. (*A*) Tissue stimulated with a narrow stream of ATP without losing laminar flow. (*B*) Tissue stimulated with a wide stream of ATP without losing laminar flow. (*C*) Confocal microscopy for observing the ATP stream profile. (*D*) Fluorescent image of the ATP stream in front of a tissue. A fluorescent dextran was used to visualize the flow. (Scale bar: 100 μm.) (*E*) Fluorescent image of the ATP stream behind a tissue. (*F*) Fluorescent section image of the ATP stream in front of a tissue. (*G*) Intensity profiles of the fluorescent images for the dashed lines in *D* and *E*.

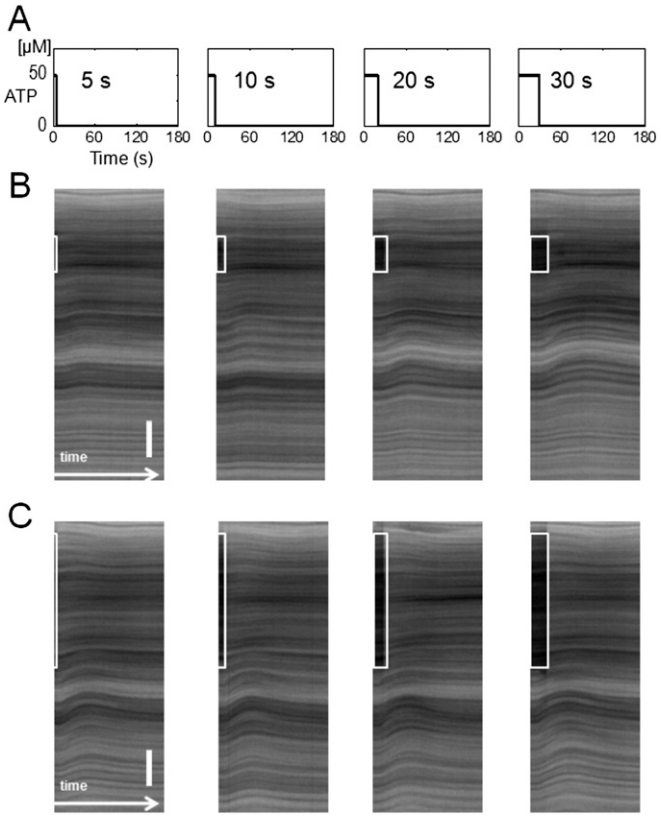

Fig. S3. Consistent rapid contraction with a time delay with slow relaxation. (*A*) Stimulation input profiles of single pulses for 5, 10, 20, and 30 s. (*B* and *C*) Kymographs show typical time response patterns for (*B*) narrow and (*C*) wide streams, although longer and wider stimulation patterns resulted in gradually longer and wider contractility responses. The varying intensity across the tissue (shown in the *y* axis of the kymograph) represents varying pigment patterns across the tissue. The darker portions of the kymograph within the white box in each figure represent area and duration of ATP stimulation because media carrying ATP included black ink as a tracer dye to visualize the extent of the ATP streams. (Scale bar: 100 μm.)

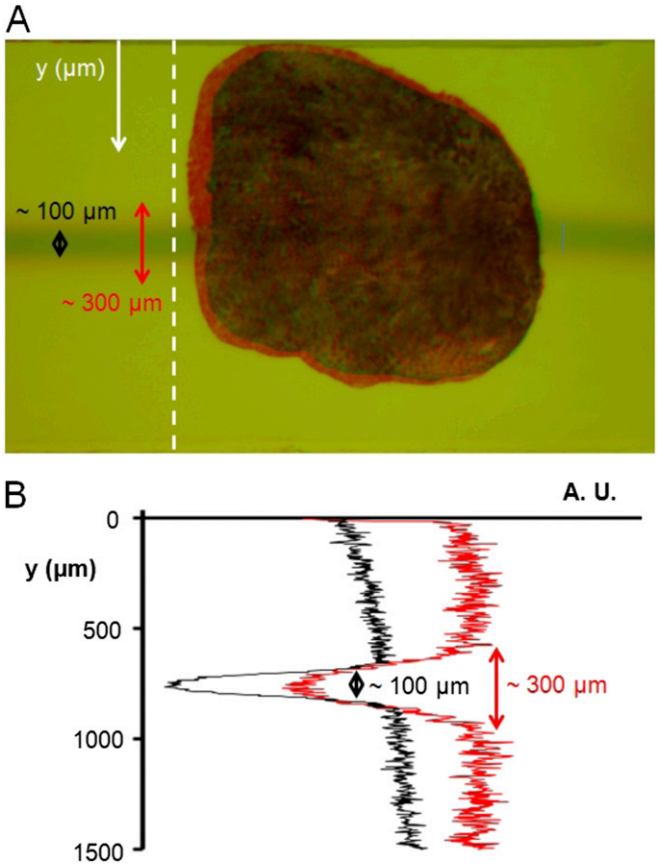

Fig. S4. BBS stream covers and extends 100 μm beyond ATP stream used in Fig. 3. Inlet pressures of the microfluidic control system were set so that the BBS stream completely covered and extended an additional 100 μm beyond the initial ATP stream. (*A*) Image merging Fig. 3 *A* and *B*: (*A, 1*) the 100-μm ATP stream (green); and (*A, 2*) the 300-μm BBS stream (red). (*B*) Intensity profile of the marker-dye along the dashed line "upstream" of the explant in *A* indicates the widths of the ATP and BBS streams.

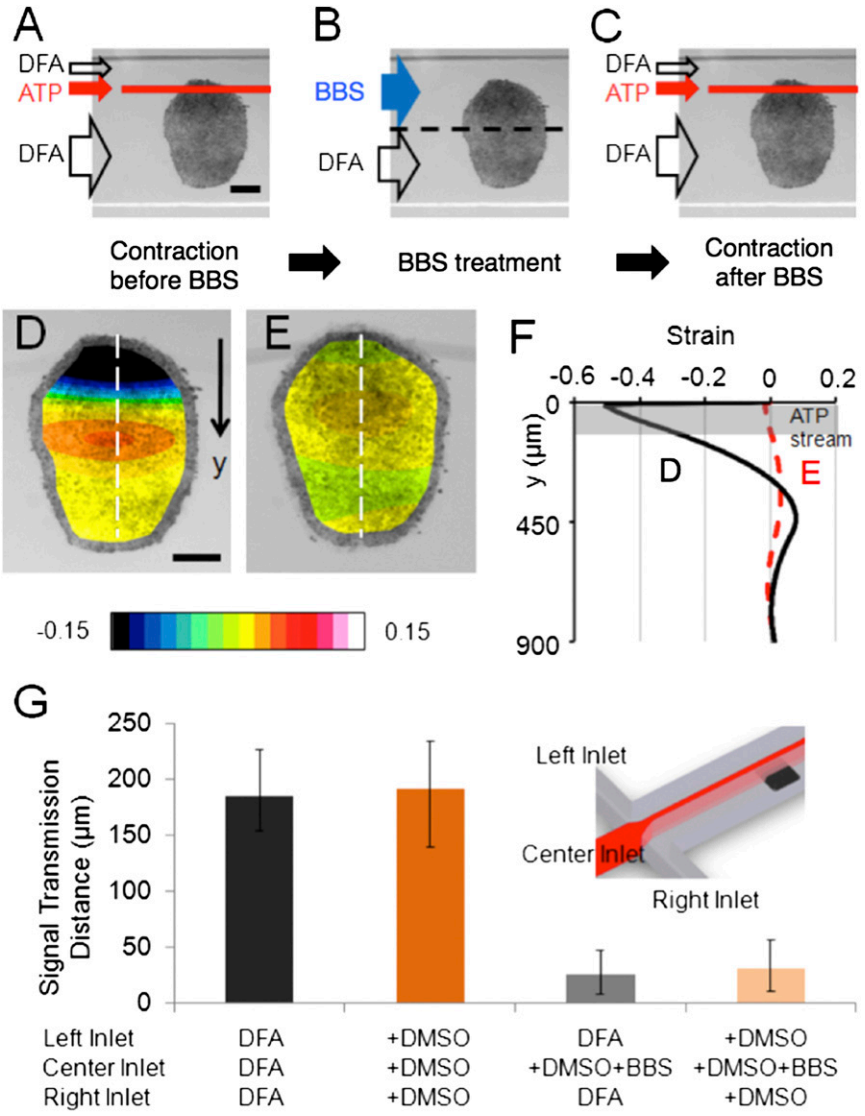

Fig. S5. Pattern of contraction depends on pattern of myosin inhibition and location of ATP stimulation. (*A*) A 20-s-duration 50-μM ATP stream was positioned at the edge of the explant and triggered localized contraction. (Scale bar: 300 μm.) (*B*) After the ATP stimulation half of the tissue was exposed to 100-μM BBS. (*C*) Following BBS exposure a 20-s pulse of ATP streamed at the same location as in *A*. (*D*) Image of a tissue overlaid with the initial ATP-stream strain map before being treated with BBS. (Scale bar: 200 μm.) (*E*) Image of the tissue overlaid with the second ATP-stream strain map after being treated with BBS. (*F*) Effect of actomyosin inhibition on strain distribution in a tissue when it was stimulated by an ATP near the edge of the tissue. The black solid line D is the strain distribution in panel *D* after the initial 100-μm stream of extracellular ATP (indicated in dark gray). The red dashed line E is the strain distribution in panel *E* after the second ATP-stream after a 2-h exposure to BBS (see *A*–*C* for the experiment procedure). (*G*) Effects of DMSO on contractile signal transmission distances after 2-h DFA, DFA + DMSO, DFA + DMSO + BBS treatments on the center inlet. Error bars represent SDs.

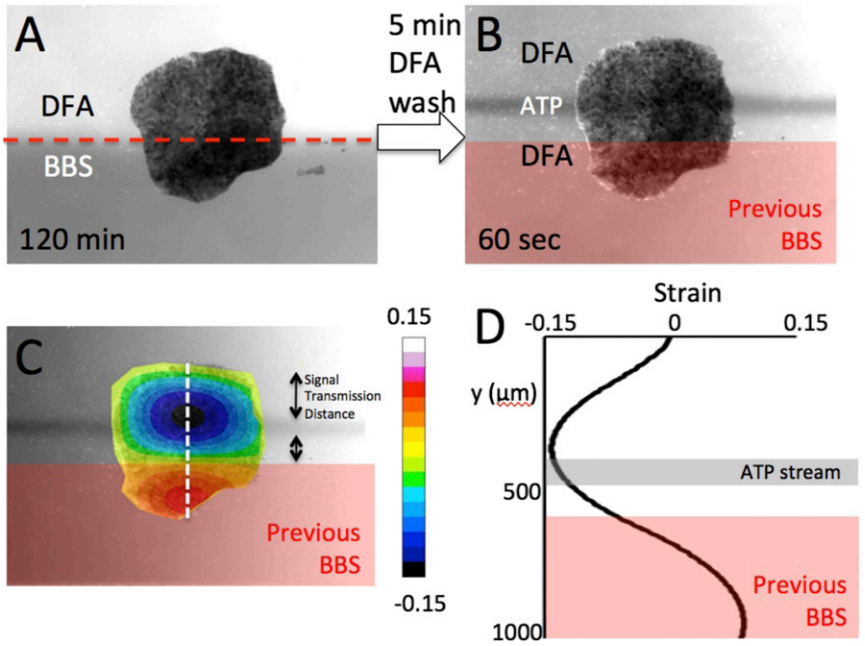

Fig. S6. BBS does not inhibit contractions beyond exposed regions. Tissue explant was cultured for 3 h in the microchannel with culture media (DFA). (*A*) Inlet pressures were adjusted and BBS was flowed over the lower portion of the tissue for 2 h. The red dashed line indicates the interface between DFA and BBS. BBS was cleared from the channel for ∼5 min with DFA. (*B*) A narrow 100-μm-wide ATP stream was pulsed for 60 s. The stream was positioned over the explant so the previous BBS exposure would overlap a responding contractile region but not the region exposed directly to ATP. (*C*) The strain map at time of maximal contraction indicates a strong contractile response in tissues not exposed to BBS. The contraction zone extends to the margin of the BBS exposed region. (*D*) The strain profile across the width of the tissue explant transverse to the ATP stream (white dashed line in *C*). The black solid line is the maximum strain after stimulation by ATP (indicated in dark gray). The red shaded regions in *B*–*D* indicate the regions exposed by BBS in *A*.

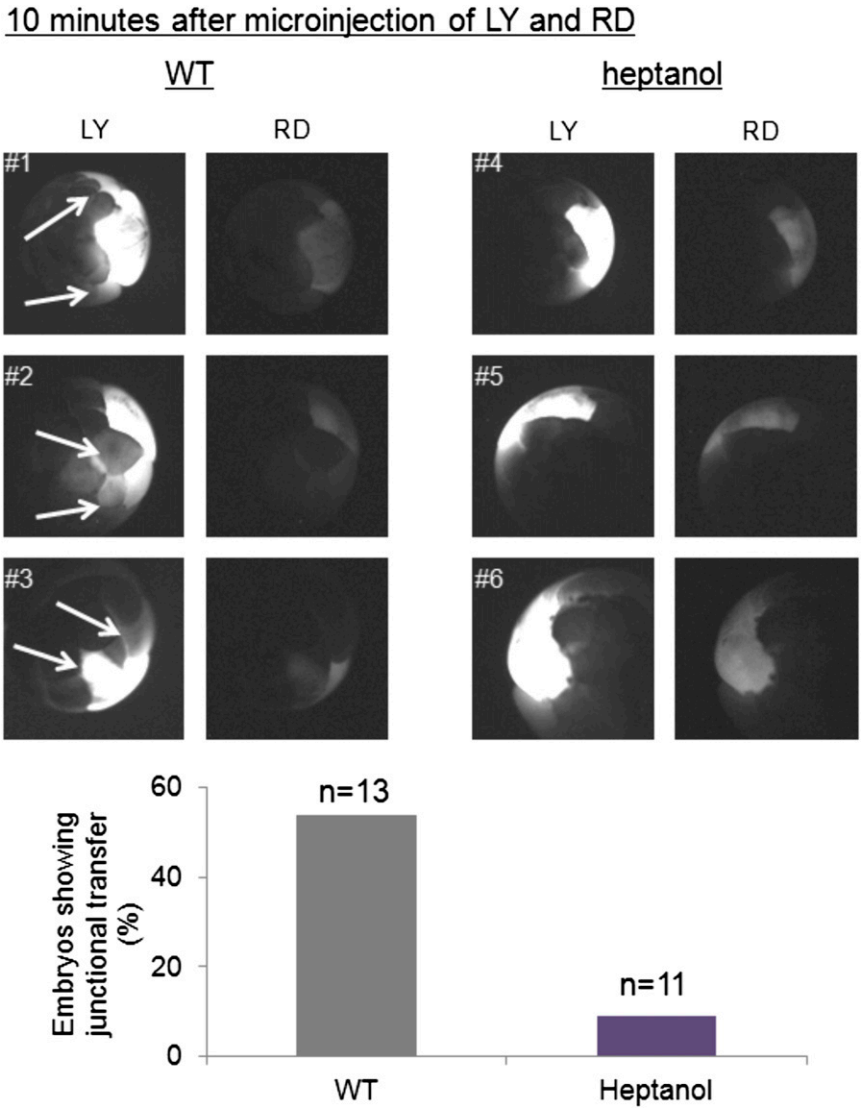

Fig. S7. HEP uncouples gap junctions. To evaluate the function of gap-junction communication and the inhibitor HEP, we looked at transfer of a small-molecular-weight dye lucifer yellow (LY) from one cell to another in the early frog embryo (1). We injected 1 blastomere in 8- or 16-cell embryos with 2:1 mixture of LY and rhodamine dextran (RD). After 10 min we monitored the diffusion of LY and RD into adjacent cells. Due to the small size of LY, gap junctions will transfer LY but not RD. Incompletely divided or injured cells will transfer both LY and RD. Control embryos (WT) showed the transfer of LY into neighboring cells (arrows) whereas the embryos treated with 50-nM HEP showed significantly less transfer. Gap-junction communication was quantified as percentage of embryos that exhibited selective transfer of LY to neighboring cells 10 min after microinjection of LY and RD, indicating that gap junctions were uncoupled by HEP.

1. Levin M, Mercola M (1998) Gap junctions are involved in the early generation of left-right asymmetry. *Dev Biol* 203(1):90–105.

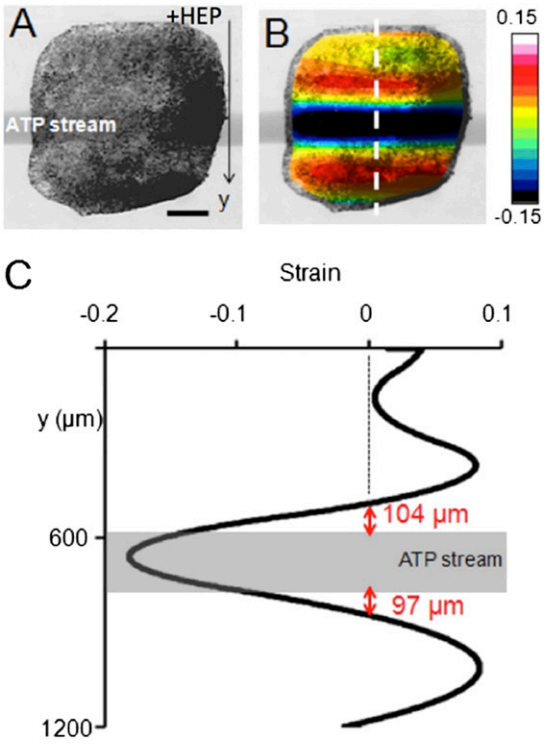

Fig. S8. Contractile signals regulated through gap junctions. (*A*) Due to the long treatment time needed for gap-junction inhibition by HEP, whole embryos were incubated in HEP before tissues were microsurgically removed. HEP was kept in the culture medium throughout microsurgery and loading of the explant into the microfluidic chamber. Contraction within a representative explant was triggered with a central ATP stream for 20 s. (Scale bar: 200 μm.) (*B*) Image of a tissue overlaid with the strain map when the tissue contracted after being treated with HEP for 5 h. (*C*) Strain distribution shown in a profile transverse to the stream (dashed line in *B*; *y* position indicated from the "top" of the tissue). The signal transmission distance is the distance between the edge of the ATP stream and the location where the strain profile crosses zero.

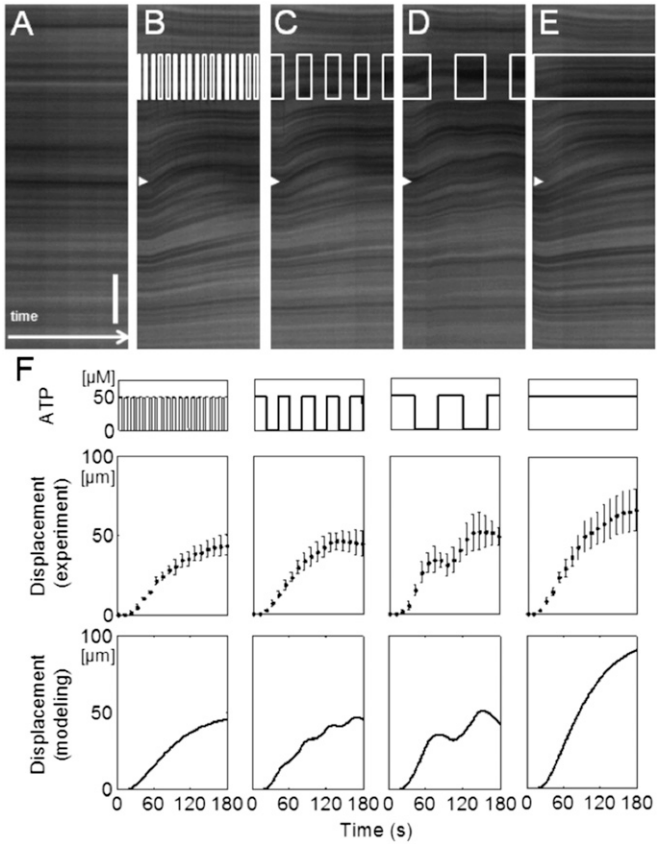

Fig. S9. Localized contractile responses of an embryonic tissue to oscillatory stimulation with controlled extracellular ATP stimulation patterns. (*A*–*E*) Kymographs showing the contractile responses after time-varying stimulation profiles: (*A*) no stimulation, (*B*) 10-s duty cycles, (*C*) 40-s duty cycles, (*D*) 80-s duty cycles, and (*E*) continuous stimulation. (Time scale bar: 180 s; vertical scale bar: 200 μm.) The arrowheads at the vertical center of the images (*B*–*E*) represent the locations where we quantify local displacement. (*F*) Quantification and simulation of the contractile responses in *B*–*E*; input ATP stimulation profiles, experimentally measured displacements, and model simulated displacements (at the locations indicated by arrowheads in *B*–*E* over time. The error bars in measured displacements represent SDs ($n = 3$).

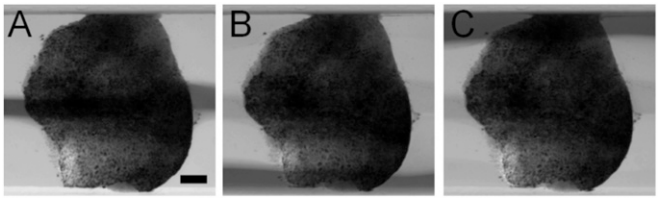

Fig. S10. Sweeping frequency stimulation creates a wave-like motion by coordinating the temporal dependence of signal propagation with the timing of the contractile response. (*A*–*C*) An ATP stream (indicated by gray color in the image) is located at the vertical center (*A*), bottom edge of the channel (*B*), and the upper edge of the channel (*C*). (Scale bar: 200 μm.)

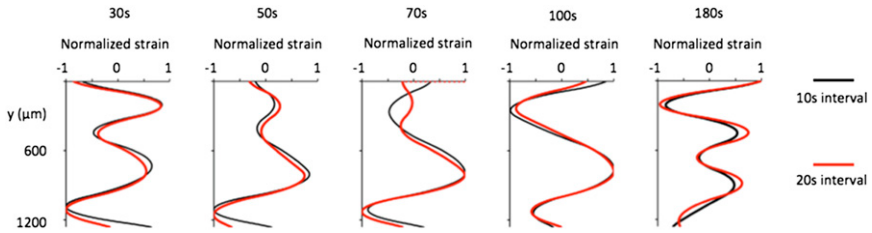

Fig. S11. Side-by-side comparison of normalized strain distributions for the strain maps (Fig. 4 *C* and *D*) after 10-s (black) and 20-s (red) interval periodic stimulation after 30, 50, 70, 100, and 180 s.

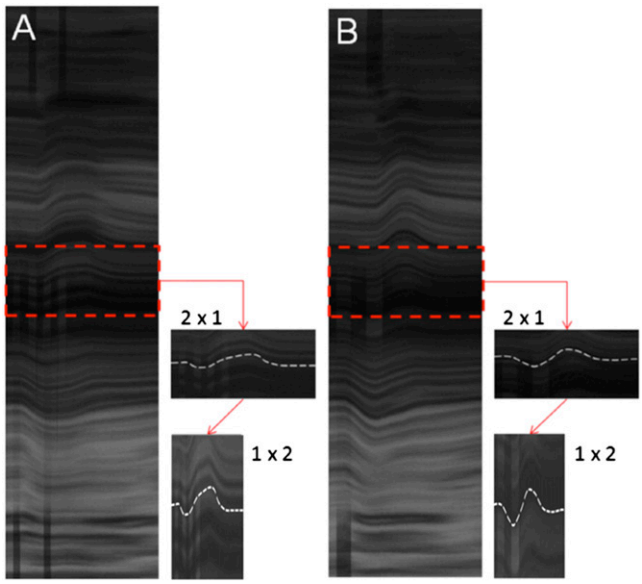

Fig. S12. Contractile wave-like patterns from kymographs shown in Fig. 4 *A* and *B*. Kymographs showing spatially and temporally varied tissue contractions in response to periodic, spatially varying ATP stimulation at (*A*) 10- and (*B*) 20-s intervals. (Fig. 4 *G* and *H*). Wave patterns were sampled from the central region of the kymographs and normalized in the *x*- and *y* directions to compare the wave shapes.

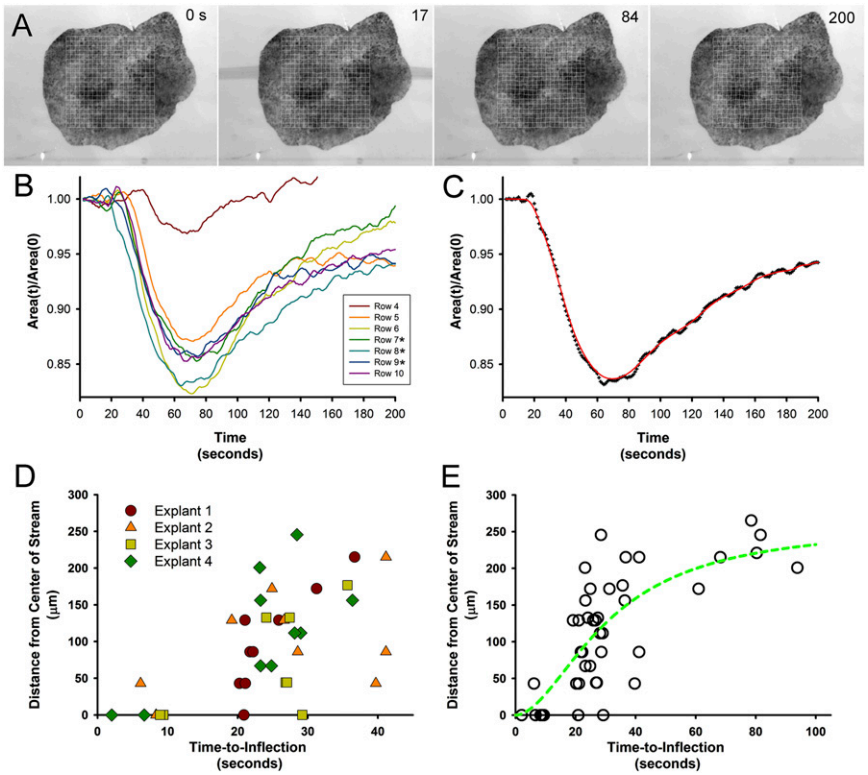

Fig. S13. Wave velocity of contractile waves. (*A*) Sequence of images captured from a representative time lapse of the explant responding to a short-duration, narrow stream of ATP. A 20-row × 20-column grid (white; each square grid element is 45 μm on a side) is superimposed over the individual frames at the start of the sequence (0 s), as the ATP stream passes over the explant (17 s), at the time of maximum contraction (84 s), and after the explant relaxes to the original position (200 s). (*B*) The areas in the grid are tracked with custom image analysis software, and the changes in the average area are calculated for each row. Note that areas are plotted only for rows that exhibit a contraction (4–10; * marks rows 7–9 that are stimulated directly by ATP). (*C*) The change in area for each row is fit with a spline function. Here, the area change and fitted spline (red) are shown for row 8. (*C*) The time that the wave passes through cells within a row is determined by the time of inflection, i.e., when the second time derivative of the spline is zero. (*D*) The time of inflection for each contractile row from four explants is plotted at their distance from the center of the ATP stream. (*E*) Wave velocity is estimated from the relationship between the time of inflection and the distance from the ATP stream. Due to the nonlinear dependence of contraction distance with time, we used statistical software (SigmaPlot v. 10; Systat Software Inc.) to examine the data from all four explants with a three-parameter sigmoidal curve [green; $f(t) = a*t^b/(c^b + t^b)$; where a is 260 μm, b is 1.83, and c is 31; $R = 0.75$, adjusted $R^2 = 0.53$]. The contraction wave velocity is estimated at ∼5 μm/s. The contraction takes 15 s to reach cells 50 μm from the center of the stream and 37 s to reach cells at 150 μm from the center of the stream. Previous studies from our group have found that the typical time constant during creep (e.g., τ) is ∼60 s (3, 4). From creep tests carried out in previous studies, we calculate the coefficient of viscosity of this material as ∼2,000 Pa·s. We find the tissue should support the propagation of a 5-μm/s wave.

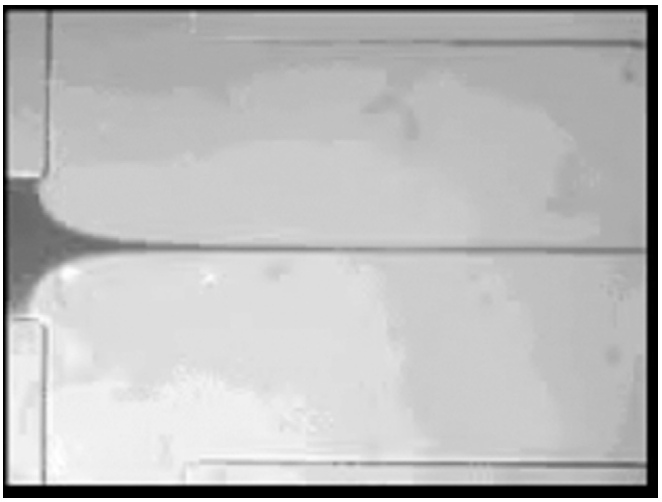

Movie S1. Performance of microfluidic control of the central stream of ATP in response to a sinusoidal reference input.

Movie S1

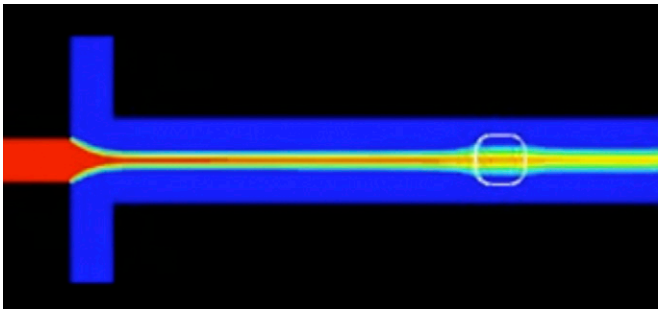

Movie S2. Computational fluid dynamics simulation predicting flow patterns in and around a tissue when controlling the position and width of the stream.

Movie S2

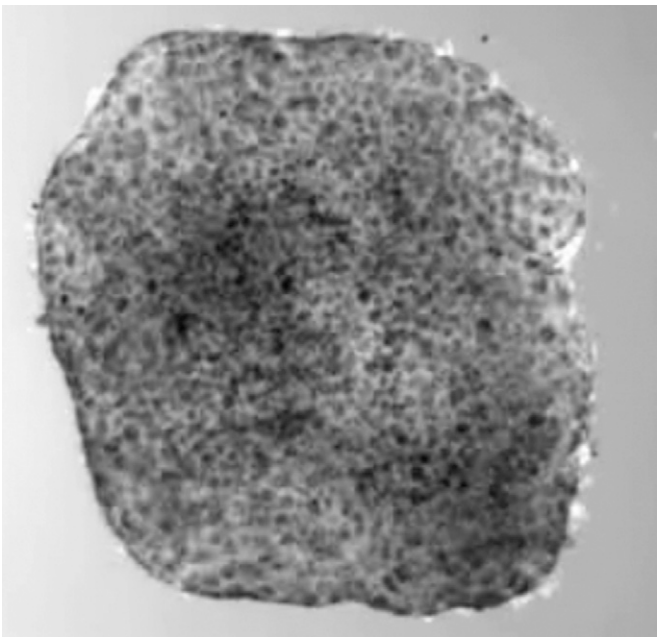

Movie S3. Localized contraction triggered by application of extracellular ATP stream for 10 s.

Movie S3

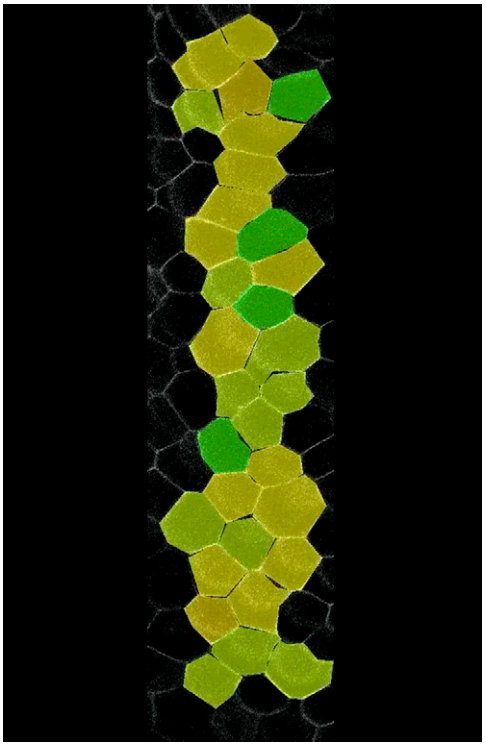

Movie S4. Confocal time-lapse movie showing individual contraction of multiple cells in response to a local stream of ATP. Cell membranes are labeled by a membrane-targeted GFP. Because the apical surfaces of the explant are not flat, we collected confocal stacks at 25-s intervals. Single frames of the movie are the product of a maximal projection of each of these stacks.

Movie S4

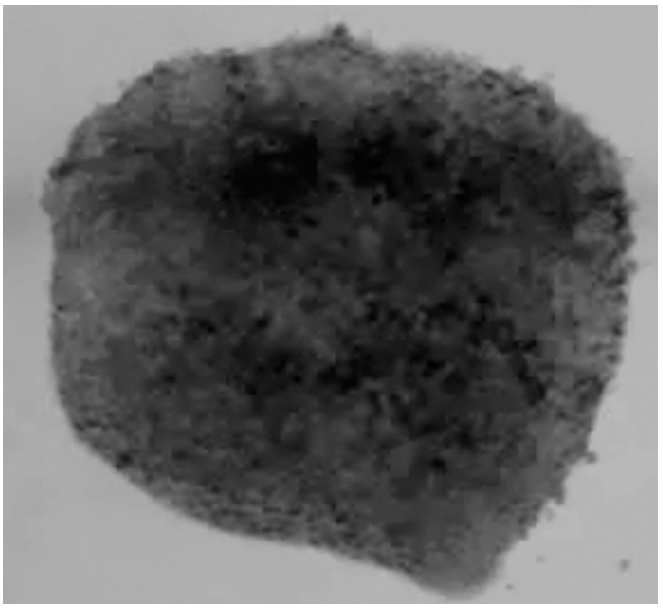

Movie S5. Localized contraction triggered by a 20-s-duration ATP stream positioned at the edge of the tissue explant.

Movie S5

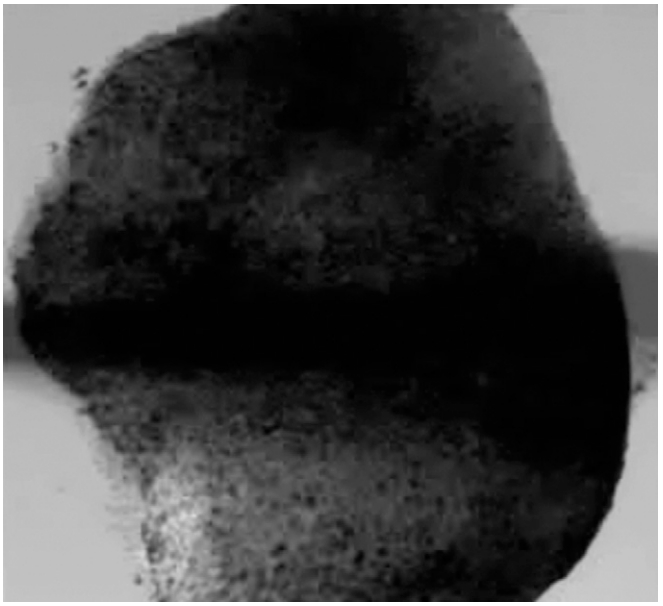

Movie S6. Oscillatory patterns of contraction in response to 10-s periodic stimulation.

Movie S6

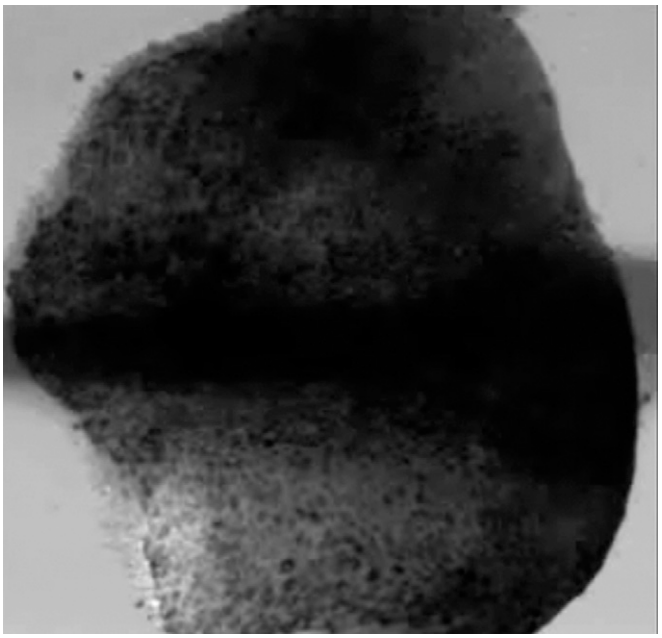

Movie S7. Oscillatory patterns of contraction in response to 20-s periodic stimulation.

Movie S7